

# Double-EIT Ground-State Cooling of Stationary Two-Dimensional Ion Lattices

Mu Qiao<sup>1,\*</sup>, Ye Wang<sup>1,2</sup>, Zhengyang Cai<sup>1</sup>, Botao Du<sup>1,4</sup>, Pengfei Wang<sup>1</sup>,  
Chunyang Luan<sup>1</sup>, Wentao Chen<sup>1</sup>, Heung-Ryoul Noh<sup>3</sup>, and Kihwan Kim<sup>1†</sup>

<sup>1</sup> *Center for Quantum Information, Institute for Interdisciplinary Information Sciences,  
Tsinghua University, Beijing 100084, P. R. China*

<sup>2</sup> *Department of Electrical and Computer Engineering, Duke University, Durham, NC 27708, USA*

<sup>3</sup> *Department of Physics, Chonnam National University, Gwangju, 61186, Korea*

<sup>4</sup> *Department of Physics and Astronomy, Purdue University, West Lafayette, IN 47907, USA*

(Dated: March 24, 2020)

We theoretically and experimentally study the electromagnetically-induced-transparency (EIT) cooling of two-dimensional ion lattices in a Paul trap. We realize the EIT ground-state cooling with  $^{171}\text{Yb}^+$  ions with hyperfine-energy levels different from other ions with a simple  $\Lambda$ -scheme that has already been used. We observe a cooling rate  $\dot{n} = 3 \times 10^4$  quanta/s and a cooling limit  $\bar{n} = 0.06 \pm 0.059$  for a single ion. The measured cooling rate and limit are consistent with theoretical predictions. We apply the double-EIT cooling on two-dimensional (2D) lattices with up to 12 ions and observe an average phonon number of  $\bar{n} = 0.82 \pm 0.34$  for the center of mass mode. Different from the 2D crystal in the Penning trap, cooling rates of multiple ions are similar to that of a single ion. The ground-state cooling of a 2D lattice with a large number of  $^{171}\text{Yb}^+$  ions will advance the field of the quantum simulation of 2D systems. Our method can also be extended to the other hyperfine qubits.

Cooling down mechanical oscillators into ground states enabled experimental investigation and applications with atoms and ions for quantum information science, including quantum metrology and quantum computation [1]. Quantized vibrations of mechanical oscillators can be resources for continuous-variable quantum computation [2–6] or Boson sampling [7–12], which begins with ground state preparation. Experimental demonstration of such applications showing quantum advantages requires the ground state cooling of dozens of vibrational modes [7].

Ground-state cooling of vibrational degrees of freedom can also enhance the performance of quantum operations with atoms and ions. Phase noises and fluctuations of qubit-qubit interaction strengths introduced by thermal motions of ions or atoms can also be suppressed by ground-cooling, which is important for realizing the high-fidelity quantum gates [13, 14] and reliable quantum simulations [15, 16]. Moreover, quantum simulation using both vibrational and fermionic degrees of freedom [17, 18] naturally demands the ground state cooling of vibrational modes. In the current race of quantum technology, the size of the quantum systems that can be manipulated in the quantum regime is scaling up, which requires simultaneous cooling of multiple mechanical oscillators.

The laser cooling provides a practical way to prepare the quantum ground state of a mechanical oscillator with atoms and ions, and even mesoscopic or macroscopic oscillator by removing the entropy from the oscillators to the photons. Laser cooling is first demonstrated using velocity-dependent radiative force [19, 20], which is called as Doppler cooling. The final temperature that

can be achieved in Doppler cooling is limited by the natural linewidth of the atoms being cooled. Sisyphus cooling can provide lower temperature than the Doppler limit [21, 22]. While Sisyphus cooling has been widely used with neutral atoms, it is hard to cool down to the ground state and suffering from slow cooling speed for trapped ions [22]. The ground state cooling can be realized by resolved-sideband cooling [23, 24]. However, the narrow excitation range of the resolved-sideband transition makes it difficult to perform ground-state cooling for a large number of motional modes with multiple ions. Moreover, some of sideband transitions are driven by high power lasers and induce charging problem [25], which is much worse for UV laser beams.

Electromagnetically-Induced-Transparency (EIT) cooling [26–28] can provide an alternative possibility that can apace cool down a wide range of vibrational modes simultaneously and has been demonstrated in the linear trap and Penning trap with tens to hundreds of ions [29, 30]. The typical EIT cooling utilizes the quantum interference emerged in three-level  $\Lambda$ -system and has been demonstrated only in ions without clock states. Here, we demonstrate a novel cooling method for  $^{171}\text{Yb}^+$  ions with clock state, based on the double EIT [31–36] in a four-level system instead of three-level. The double-EIT cooling has been theoretically studied [37–40] without experiment realizations. We experimentally perform the double-EIT cooling of  $^{171}\text{Yb}^+$  ions to prepare ground states of all the transverse motional modes in a two-dimensional(2D) ion crystal [41]. We systematically study the efficiency of EIT cooling depending on various control parameters including intensities and detunings of probe and driving laser beams and find optimal conditions. For multiple motional mode, we cool the crystal near to the ground state in a couple of hundreds microseconds, which is similar to that of a

\* mu.q.phys@gmail.com

† kimkihwan@mail.tsinghua.edu.cn



between  $|\pm\rangle \leftrightarrow |e\rangle$ . The other beam, EIT 2, works as probe beam coupling to the transition  $|0\rangle \leftrightarrow |e\rangle$ . The detuning  $\Delta_p$  of the probe beam is fixed at  $(2\pi)55.6$  MHz, and the detuning  $\Delta_d$  of the driving beam is adjusted by varying the frequency difference between two AOMs. As shown in Fig. 1(c), the EIT 1 passes through two AOMs to adjust  $\Delta_d$ . We measure the Rabi frequencies and the polarization of the probe and driving beams by observing the differential ac Stark shift of the qubit transition and the Zeeman state qubits [22, 43] [Appendix E]. The Rabi frequencies,  $\{\Omega_{\sigma_-}, \Omega_{\pi}, \Omega_{\sigma_+}\}/(2\pi)$ , of the driving beam of  $24\mu\text{W}$  and probe beam of  $5.5\mu\text{W}$  are  $\{16.74, 1.72, 18.03\}$  MHz and  $\{1.49, 6.67, 3.17\}$  MHz.

Fig. 2 (a) shows the experimental sequence to study the EIT cooling with a single ion. For a single  $^{171}\text{Yb}^+$  ion, we use the trap frequency of  $\omega_y/2\pi = 2.38$  MHz along of the transverse direction and  $\{\omega_x, \omega_z\}/2\pi = \{0.42, 0.47\}$  MHz in the crystal plane. We first apply Doppler cooling, which leads to Doppler-limit temperatures of the motional modes around the mean phonon number  $\bar{n} \approx 7$ . After Doppler cooling, 95% population of the internal state of the ion falls into the  $S_{1/2}|F=1\rangle$  manifold, which the EIT cooling involves. We then apply EIT beams for a duration  $\tau_{\text{EIT}}$ . To measure the final phonon number  $\bar{n}$ , we first apply  $3\mu\text{s}$  optical pumping to prepare the ground state  $S_{1/2}|F=0, m=0\rangle$ . Then we drive blue sideband transition, and we extract  $\bar{n}$  by fitting the time evolution of it [44].

We experimentally study the EIT cooling dynamics with the optimized relative detuning,  $\Delta_d - \Delta_p$ , by measuring the mean phonon number  $\bar{n}$  at various cooling duration  $\tau_{\text{EIT}}$ , as indicated in Fig. 2 (b). We measure  $\bar{n}$  by fitting the blue sideband transitions, which are shown in Fig. 2 (c) before and (d) after EIT cooling. Without EIT cooling, the blue sideband transition decays fast due to the various excitation on different vibrational modes with different Rabi frequencies. The minimum value of  $\bar{n}_{\text{min}}=0.06$  reached by EIT cooling shown in Fig. 2 (d) demonstrates a near ground state cooling similar to the sideband cooling. The  $1/e$  cooling time  $\tau_{\text{cool}} = 1/\gamma_{\text{cool}}$ , where  $\gamma_{\text{cool}}$  is cooling rate, is  $25\mu\text{s}$ . The duration of  $200\mu\text{s}$  is sufficient to reach the ground state.

The optimal cooling condition and cooling range of the double-EIT are studied by changing the relative detuning of the EIT beams. The efficiency of the EIT cooling is determined by the ratio of absorption strengths between red-sideband and blue-sideband transitions, as shown in Fig. 1(b), which is controlled by the detuning of the driving beam  $\Delta_d$  in our experiment.

We observe the optimal detuning  $(\Delta_p - \Delta_d)/(2\pi)$  for the EIT cooling locates at  $4.55$  MHz. This value is in good agreement with the predicted value of  $4.57$  MHz, which can be calculated by  $\delta_B + \delta_{\text{DR}} - \nu$ , where  $\delta_{\text{DR}} = (2\pi) 2.31$  MHz is dressed-state ac Stark shift [Appendix B, C]. We also performed a numerical simulation of the cooling range, including the heating rate of  $0.67$  quanta/ms of the trap. The average phonon number from the simulation are indicated as solid line in Fig. 2 (e) and are in good

agreement with our experimental results.

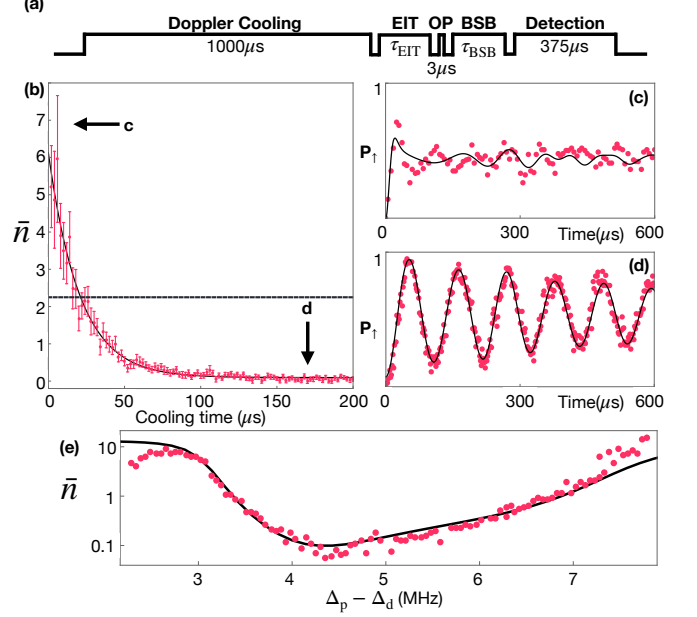


FIG. 2. (a) Experimental sequence to study the efficiency of EIT cooling of a single trapped ion. (b) Cooling dynamics for the transverse mode of y-direction. Red points are experimental data obtained by fitting blue-sideband transitions shown in (c) and (d). Here, error bars are fitting errors. The black line is fitting curve by an exponential decay function. The horizontal dashed line indicates  $1/e$  of initial phonon number. (c,d) The blue-sideband transition after (c) Doppler cooling and (d) EIT cooling of  $200\mu\text{s}$ . (e) Average phonon number  $\bar{n}$  at the end of the EIT cooling depending on the relative detuning between the probe beam and the driving beam. The black line is the numerical simulation results by solving the master equation.

We also experimentally study the EIT cooling rate,  $\gamma_{\text{cool}}$  and minimum phonon number  $n_{\text{min}}$  depending on intensities of driving and probe beams as shown in Fig. 3. We vary the powers of the driving beam and the probe beam with the probe beam of  $5.5\mu\text{W}$  ( $\Omega_p/2\pi = 6.67$  MHz) and the driving beam of  $24\mu\text{W}$  ( $\Omega_d/2\pi = 17.39$  MHz), respectively. We note that we search the optimal EIT detuning  $(\Delta_p - \Delta_d)$  at each point of laser powers. As shown in Fig. 3(a), by increasing the power of the driving beam up to our experimental limitation, we observe the enhancement of cooling effect with high cooling rate and low cooling limit. We find that there is an optimal value for the Rabi frequency of the probe beam.

To investigate the EIT cooling effect on a large ion crystal, we hold a 2D crystal formed by 12 ions in a pancake harmonic potentials [41] with trap frequencies  $\{\omega_x, \omega_y, \omega_z\}/(2\pi) = \{0.34, 1.22, 0.42\}$  MHz. The efficiency of the EIT cooling on the large crystal is assessed by comparing the ratio of red-sideband and blue-sideband transition from the Raman spectrum before and after EIT cooling. Fig. 4 (a) is the spectrum with only Doppler cooling, where the peaks of blue sideband (blue

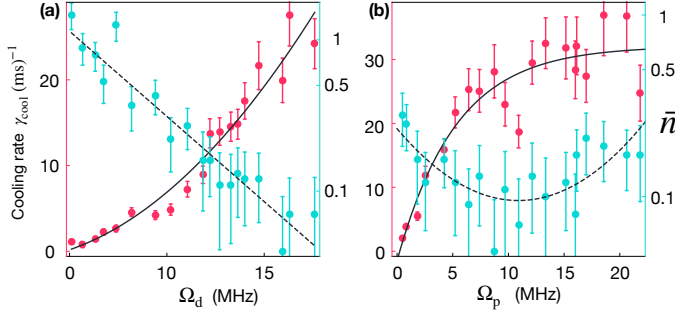


FIG. 3. (a) and (b) show the final mean phonon numbers (red points) and cooling rates (green points) depending on the power of (a) driving beam and (b) probe beam. Error bars are from the fitting of blue-sideband transitions, similar to Fig. 2(c,d). Solid lines are empirical fittings to guide the dependency.

curve) and red sideband (red curve) transitions have similar heights across all the motional modes, which indicates the phonon numbers are much larger than 1. Fig. 4 (b) shows the spectrum after Doppler and EIT cooling. The disappearance of red-sideband transitions indicates the simultaneous ground state cooling of all the modes. The small peak in the spectrum of red sideband transitions comes from not perfect ground-state cooling of center of mass (COM) mode due to the high heating rate with 12 ions. We numerically simulate the red-sideband absorption spectrum of the crystal in the vicinity of each mode for the parameters of our experiment [29]. The estimated phonon numbers of COM mode is  $1.04 \pm 0.26$  [Appendix F].

We also use the optical-dipole-force (ODF) thermometry [45] to measure the final phonon number of COM mode. The ODF, which is realized by simultaneously applying red-sideband and blue-sideband transitions, generates a  $\sigma_x \sigma_x$  interaction, where the decoherence from ion-phonon coupling appears in the x basis. We use the Ramsey measurement to probe this decoherence, as shown in Fig. 4(c). We first prepare all the qubits to its ground state in  $\sigma_z$  basis,  $|\downarrow\rangle_z$ , then apply the ODF for two fixed duration  $\tau_{\text{ODF}}$  with a spin-echo pulse sandwiched in between. Near the COM mode of 12 ions, we obtain the spectrum depending on the detuning  $\mu_R$  of ODF beams, as shown in Fig. 4 (d). We can estimate the temperature of the crystal by fitting the spectrum to the formula in [Appendix G] [45], where the  $\bar{n}$  of Doppler cooling and EIT cooling are  $9.97 \pm 4.86$  and  $0.82 \pm 0.34$ , respectively. Here, we calibrate the strength of ODF beams with a single ion, whose temperature is also accurately measured by fitting the blue-sideband transition.

We also investigate the EIT cooling dynamics for the COM mode of 12 ions, and compare it for the case of a single ion, as shown in Fig. 4 (e). We develop a simple method to estimate  $\bar{n}$  instead of using the whole ODF spectrum in Fig. 4(d). We find the relation between  $\bar{n}$  and the heights of the ODF signal at the detuning with

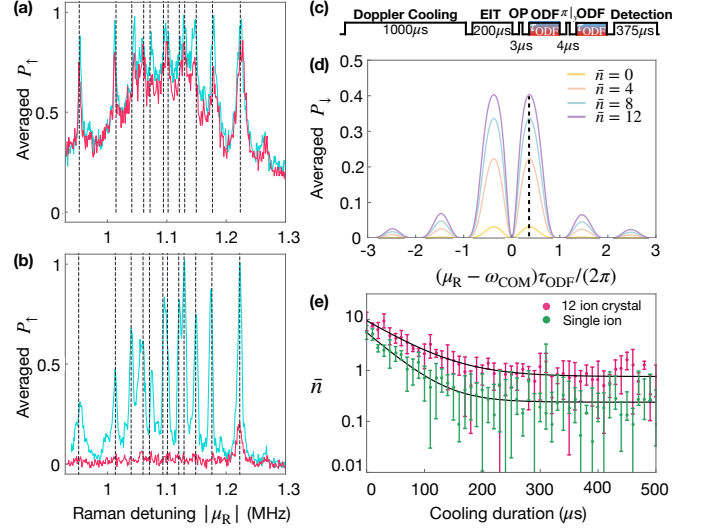


FIG. 4. (a,b) Blue (blue curve) and red-sideband (red curve) spectrum after (a) Doppler cooling and (b) EIT cooling. The horizontal axis  $\mu_R = \omega_R - \omega_0$  is the detuning of the Raman transition from the qubit transition. Dashed lines indicate the locations of 12 motional modes perpendicular to the 2D-crystal plane. (c) Pulse sequence for the ODF thermometry. (d) ODF spectrum with different average phonon number. The dashed black line indicates the position we choose for the cooling rate measurement. (e) Cooling dynamics for the single ion (green) and 12 ions in 2D crystal (red). Dots are experimental data with error bars representing the standard deviation of the phonon number measurements due to the quantum projection noise. Solid lines are fitting curves by exponential decay functions.

the largest decoherence [Appendix G], which is used to convert the heights of the ODF signal to the corresponding  $\bar{n}$ . We observe the cooling speed of 12 ions is as fast as that of a single ion shown in Fig. 4(e). We do not observe the enhancement of cooling speed as the number of ions increase [30, 46], which would come from the difference between stationary and rotating nature of 2D crystal.

In this paper, we provide the experimental evidence that EIT cooling can be performed with  $^{171}\text{Yb}^+$  ions and used for the efficient ground-state cooling of all the motional modes in 2D crystal. Our demonstration shows the possibility that EIT cooling can be realized for atoms and ions with more complicated level structures than  $\Lambda$ -scheme. We believe this fast ground-state cooling will be the essential experimental building block with a large number of ions for quantum simulation including quantum magnetism, quantum chemistry, and quantum machine learning.

## ACKNOWLEDGEMENT

We thank Paul Haljan, Dzmitry Matsukevich, Yiheng Lin, John Bollinger, Athreya Shankar, and Christian

Roos for their helpful discussion. We acknowledge the use of the Quantum Toolbox in PYTHON (QuTiP)[47]. This work was supported by the National Key Research and Development Program of China under Grants No.

2016YFA0301900 and No. 2016YFA0301901 and the National Natural Science Foundation of China Grants No. 11374178, No. 11574002, and No. 11974200.

- 
- [1] D. J. Wineland, *Rev. Mod. Phys.* **85**, 1103 (2013).
  - [2] S. Lloyd and S. L. Braunstein, *Phys. Rev. Lett.* **82**, 1784 (1999).
  - [3] H.-K. Lau and M. B. Plenio, *Phys. Rev. Lett.* **117**, 100501 (2016).
  - [4] S. Ding, G. Maslennikov, R. Häblützel, H. Loh, and D. Matsukevich, *Phys. Rev. Lett.* **119**, 150404 (2017).
  - [5] S. Ding, G. Maslennikov, R. Häblützel, and D. Matsukevich, *Phys. Rev. Lett.* **119**, 193602 (2017).
  - [6] C. Flühmann, T. L. Nguyen, M. Marinelli, V. Negnevitsky, K. Mehta, and J. Home, *Nature* **566**, 513 (2019).
  - [7] S. Aaronson and A. Arkhipov, *Proceedings of the 43rd annual ACM symposium on Theory of computing - STOC '11*, 333 (2011).
  - [8] H.-K. Lau and D. F. V. James, *Phys. Rev. A* **85**, 062329 (2012).
  - [9] C. Shen, Z. Zhang, and L.-M. Duan, *Phys. Rev. Lett.* **112**, 050504 (2014).
  - [10] K. Toyoda, R. Hiji, A. Noguchi, and S. Urabe, *Nature* **527**, 74 (2015).
  - [11] M. Um, J. Zhang, D. Lv, Y. Lu, S. An, J.-N. Zhang, H. Nha, M. Kim, and K. Kim, *Nat. Commun.* **7**, 1 (2016).
  - [12] Y. Shen, Y. Lu, K. Zhang, J. Zhang, S. Zhang, J. Huh, and K. Kim, *Chem. Sci.* **9**, 836 (2018).
  - [13] C. Ballance, T. Harty, N. Linke, M. Sepiol, and D. Lucas, *Phys. Rev. Lett.* **117**, 060504 (2016).
  - [14] T. Harty, M. Sepiol, D. Allcock, C. Ballance, J. Tarlton, and D. Lucas, *Phys. Rev. Lett.* **117**, 140501 (2016).
  - [15] R. Blatt and C. F. Roos, *Nature Physics* **8**, 277 (2012).
  - [16] C. Monroe, W. Campbell, L.-M. Duan, Z.-X. Gong, A. Gorshkov, P. Hess, R. Islam, K. Kim, G. Pagano, P. Richerme, *et al.*, *arXiv preprint arXiv:1912.07845* (2019).
  - [17] A. Mezzacapo, J. Casanova, L. Lamata, and E. Solano, *Phys. Rev. Lett.* **109**, 200501 (2012).
  - [18] D. Lv, S. An, Z. Liu, J.-N. Zhang, J. S. Pedernales, L. Lamata, E. Solano, and K. Kim, *Physical Review X* **8**, 021027 (2018).
  - [19] D. J. Wineland, R. E. Drullinger, and F. L. Walls, *Phys. Rev. Lett.* **40**, 1639 (1978).
  - [20] W. Neuhauser, M. Hohenstatt, P. Toschek, and H. Dehmelt, *Phys. Rev. Lett.* **41**, 233 (1978).
  - [21] J. Dalibard and C. Cohen-Tannoudji, *JOSA B* **6**, 2023 (1989).
  - [22] S. Ejtemaee and P. Haljan, *Phys. Rev. Lett.* **119**, 043001 (2017).
  - [23] C. Monroe, D. Meekhof, B. King, S. R. Jefferts, W. M. Itano, D. J. Wineland, and P. Gould, *Phys. Rev. Lett.* **75**, 4011 (1995).
  - [24] C. Roos, T. Zeiger, H. Rohde, H. Nägerl, J. Eschner, D. Leibfried, F. Schmidt-Kaler, and R. Blatt, *Phys. Rev. Lett.* **83**, 4713 (1999).
  - [25] M. Harlander, M. Brownnutt, W. Hänsel, and R. Blatt, *New Journal of Physics* **12**, 093035 (2010).
  - [26] G. Morigi, J. Eschner, and C. H. Keitel, *Phys. Rev. Lett.* **85**, 4458 (2000).
  - [27] C. Roos, D. Leibfried, A. Mundt, F. Schmidt-Kaler, J. Eschner, and R. Blatt, *Phys. Rev. Lett.* **85**, 5547 (2000).
  - [28] Y. Lin, J. P. Gaebler, T. R. Tan, R. Bowler, J. D. Jost, D. Leibfried, and D. J. Wineland, *Phys. Rev. Lett.* **110**, 153002 (2013).
  - [29] R. Lechner, C. Maier, C. Hempel, P. Jurcevic, B. P. Lanyon, T. Monz, M. Brownnutt, R. Blatt, and C. F. Roos, *Physical Review A* **93**, 053401 (2016).
  - [30] E. Jordan, K. A. Gilmore, A. Shankar, A. Safavi-Naini, J. G. Bohnet, M. J. Holland, and J. J. Bollinger, *Phys. Rev. Lett.* **122**, 053603 (2019).
  - [31] E. Paspalakis and P. Knight, *Journal of Optics B: Quantum and Semiclassical Optics* **4**, S372 (2002).
  - [32] S. Beck and I. E. Mazets, *Physical Review A* **95**, 013818 (2017).
  - [33] H. M. Alotaibi and B. C. Sanders, *Physical Review A* **89**, 021802 (2014).
  - [34] B. S. Ham and P. R. Hemmer, *Phys. Rev. Lett.* **84**, 4080 (2000).
  - [35] M.-J. Lee, J. Ruseckas, C.-Y. Lee, V. Kudriašov, K.-F. Chang, H.-W. Cho, G. Juzeliūnas, and A. Y. Ite, *Nature communications* **5**, 5542 (2014).
  - [36] D. Wang, C. Liu, C. Xiao, J. Zhang, H. M. Alotaibi, B. C. Sanders, L.-G. Wang, and S. Zhu, *Scientific reports* **7**, 5796 (2017).
  - [37] J. Evers and C. H. Keitel, *EPL (Europhysics Letters)* **68**, 370 (2004).
  - [38] Z. Yi, W.-J. Gu, and G.-X. Li, *Opt. Exp.* **21**, 3445 (2013).
  - [39] T. Huang, Y. Qi, F. Zhou, Y. Niu, and S. Gong, *Optik-International Journal for Light and Electron Optics* **127**, 2978 (2016).
  - [40] I. Semerikov, I. Zalivako, A. Borisenko, K. Khabarova, and N. Kolachevsky, *Journal of Russian Laser Research* **39**, 568 (2018).
  - [41] Y. Wang, M. Qiao, Z. Cai, K. Zhang, N. Jin, P. Wang, W. Chen, C. Luan, H. Wang, Y. Song, *et al.*, *arXiv preprint arXiv:1912.04262* (2019).
  - [42] Y. Wang, M. Um, J. Zhang, S. An, M. Lyu, J.-N. Zhang, L.-M. Duan, D. Yum, and K. Kim, *Nature Photonics* **11**, 646 (2017).
  - [43] H. Häffner, S. Gulde, M. Riebe, G. Lancaster, C. Becher, J. Eschner, F. Schmidt-Kaler, and R. Blatt, *Phys. Rev. Lett.* **90**, 143602 (2003).
  - [44] D. Leibfried, R. Blatt, C. Monroe, and D. Wineland, *Reviews of Modern Physics* **75**, 281 (2003).
  - [45] B. C. Sawyer, J. W. Britton, A. C. Keith, C.-C. J. Wang, J. K. Freericks, H. Uys, M. J. Biercuk, and J. J. Bollinger, *Phys. Rev. Lett.* **108**, 213003 (2012).
  - [46] A. Shankar, E. Jordan, K. A. Gilmore, A. Safavi-Naini, J. J. Bollinger, and M. J. Holland, *Physical Review A* **99**, 023409 (2019).

- [47] J. R. Johansson, P. D. Nation, and F. Nori, Computer Physics Communications **184**, 1234 (2013).
- [48] B. Lounis and C. Cohen-Tannoudji, Journal de Physique II **2**, 579 (1992).
- [49] D. Hayes, D. N. Matsukevich, P. Maunz, D. Hucul, Q. Quraishi, S. Olmschenk, W. Campbell, J. Mizrahi, C. Senko, and C. Monroe, Phys. Rev. Lett. **104**, 140501 (2010).

## APPENDIX

### A. The dark states

Considering the semi-classical treatment for the system of Fig. 1(a) in the rotating frame, we have the Hamiltonian

$$\hat{H} = \begin{pmatrix} 0 & \frac{\Omega_{\sigma-}}{2} & -\frac{\Omega_{\pi}}{2} & \frac{\Omega_{\sigma+}}{2} \\ \frac{\Omega_{\sigma-}}{2} & \Delta_d + \delta_B & 0 & 0 \\ -\frac{\Omega_{\pi}}{2} & 0 & \Delta_p & 0 \\ \frac{\Omega_{\sigma+}}{2} & 0 & 0 & \Delta_d - \delta_B \end{pmatrix} \quad (1)$$

where the basis is  $\{|e\rangle, |+\rangle, |0\rangle, |-\rangle\}$ ,  $\Delta_d$  is the detuning between the driving laser and  $|0\rangle$  to  $|e\rangle$  transition,  $\Delta_p$  is the detuning between the probe laser and  $|0\rangle$  to  $|e\rangle$  transition, and  $\delta_B$  is the Zeeman splitting. Here we denote  $\hbar = 1$ .

Once the detuning of the probe beam matches to one of the Zeeman level  $\Delta_p = \Delta_d + \delta_B \equiv \Delta$ , the Hamiltonian can be change to to

$$\hat{H} = \begin{pmatrix} 0 & \frac{\Omega_{\sigma-}}{2} & -\frac{\Omega_{\pi}}{2} & \frac{\Omega_{\sigma+}}{2} \\ \frac{\Omega_{\sigma-}}{2} & \Delta & 0 & 0 \\ -\frac{\Omega_{\pi}}{2} & 0 & \Delta & 0 \\ \frac{\Omega_{\sigma+}}{2} & 0 & 0 & \Delta - 2\delta_B \end{pmatrix} \quad (2)$$

This Hamiltonian gives us one dark state

$$|D_1\rangle = \frac{1}{\sqrt{\Omega_{\pi}^2 + \Omega_{\sigma-}^2}} (\Omega_{\pi} |+\rangle + \Omega_{\sigma-} |0\rangle) \quad (3)$$

And the coincidence with the other Zeeman level gives us the second dark state

$$|D_2\rangle = \frac{1}{\sqrt{\Omega_{\pi}^2 + \Omega_{\sigma+}^2}} (\Omega_{\sigma+} |0\rangle + \Omega_{\pi} |-\rangle) \quad (4)$$

### B. The scattering amplitude interpretation for the bright Resonance

We can more precisely understand this four-level atomic system interacting with laser beams by quantizing laser field, which provides the Hamiltonian written as

$$H = H_0 + V_{\sigma+} + V_{\sigma-} + V_{\pi} + \sum_v V_v, \quad (5)$$

where

$$\begin{aligned} H_0 &= E_{\sigma+} |- \rangle \langle -| + E_{\pi} |0 \rangle \langle 0| + E_{\sigma-} |+ \rangle \langle +| + E_e |e \rangle \langle e| + \omega_{\sigma-} a_{\sigma-}^{\dagger} a_{\sigma-} \\ &\quad + \omega_{\pi} a_{\pi}^{\dagger} a_{\pi} + \omega_{\sigma+} a_{\sigma+}^{\dagger} a_{\sigma+} + \sum_v \omega_v a_v^{\dagger} a_v \\ V_{\sigma+} &= \frac{d_{\sigma+}}{2} (a_{\sigma+} |e \rangle \langle -| + a_{\sigma+}^{\dagger} |- \rangle \langle e|) \\ V_{\pi} &= \frac{d_{\pi}}{2} (a_{\pi} |e \rangle \langle 0| + a_{\pi}^{\dagger} |0 \rangle \langle e|) \\ V_{\sigma-} &= \frac{d_{\sigma-}}{2} (a_{\sigma-} |e \rangle \langle +| + a_{\sigma-}^{\dagger} |+ \rangle \langle e|) \\ V_v &= \frac{d_v}{2} (a_v |e \rangle \langle -| + a_v^{\dagger} |- \rangle \langle e| + a_v |e \rangle \langle 0| + a_v^{\dagger} |0 \rangle \langle e| + a_v |e \rangle \langle +| + a_v^{\dagger} |+ \rangle \langle e|). \end{aligned} \quad (6)$$

Here, the last term represent the interaction with the vacuum field. Basically, the absorption spectra is proportional to the squared scattering amplitude of the transition

$$|i \rangle \equiv |0, 1, N_1, N_2, 0 \rangle \rightarrow |f \rangle \equiv |0, 0, N_1, N_2, 1 \rangle, \quad (7)$$

where the first index represent the atom internal state, the second number represent the Fock state of the probe field, and the last three terms represent the Fock state of  $\sigma_-$  field,  $\sigma_+$  field and vacuum field. It is worthy to remind you that the absorption spectra means the atom absorb one photon and then emit it to the vacuum, where part of it can be detected by PMT.

The scattering amplitude can be calculated by the  $T$  matrix

$$T = \langle f | V | i \rangle + \lim_{\eta \rightarrow 0_+} \left\langle f \left| V \frac{1}{E_i - H + i\eta} V \right| i \right\rangle \quad (8)$$

and due to  $V = V_{\sigma+} + V_{\sigma-} + V_{\pi} + \sum_v V_v$ ,  $V|i \rangle$  and  $V|f \rangle$  can be written by

$$V|i \rangle = \frac{\Omega_{\pi}}{2} |\varphi_e \rangle, \quad V|f \rangle = \frac{\Omega_v}{2} |\varphi_e \rangle. \quad (9)$$

where we denote  $|\varphi_e \rangle \equiv |e, 0, N_1, N_2, 0 \rangle$ . There are two states strongly coupled to  $|\varphi_e \rangle$ , which are

$$|- , 0, N_1 + 1, N_2, 0 \rangle, \quad |+ , 0, N_1, N_2 + 1, 0 \rangle, \quad (10)$$

since

$$V|+ , 0, N_1 + 1, N_2, 0 \rangle = \frac{\Omega_{\sigma-}}{2} |\varphi_e \rangle, \quad V|- , 0, N_1, N_2 + 1, 0 \rangle = \frac{\Omega_{\sigma+}}{2} |\varphi_e \rangle, \quad (11)$$

respectively. We note that the subspace is closed. We can calculate the  $T$  matrix by projecting the Hamiltonian to the subspace spanned by  $\{|+ , 0, N_1 + 1, N_2, 0 \rangle, |- , 0, N_1, N_2 + 1, 0 \rangle, |\varphi_e \rangle\}$ .

In the second order perturbation theory[48], the effective Hamiltonian in this subspace can be calculated by

$$PH_{\text{eff}}P = PH_0P + PVP + PVQ \frac{1}{E_0 - QH_0Q} QVP, \quad (12)$$



where  $P$  is the projection operator to the subspace and  $Q = 1 - P$ . After calculating all the terms, the effective Hamiltonian can be simplified by

$$\hat{H}_{\text{eff}} = \begin{pmatrix} \Delta_\pi + i\frac{\Gamma}{2} & -\frac{\Omega_{\sigma-}}{2} & -\frac{\Omega_{\sigma+}}{2} \\ -\frac{\Omega_{\sigma-}}{2} & \Delta_\pi - \Delta_{\sigma-} & 0 \\ -\frac{\Omega_{\sigma+}}{2} & 0 & \Delta_\pi - \Delta_{\sigma+} \end{pmatrix} \quad (13)$$

Therefore the fluorescence,  $W(\Delta) = |T(\Delta)|^2$ , which is proportional to the square of the scattering amplitude is

$$W(\Delta_\pi) = \frac{16(\Delta_\pi - \Delta_{\sigma-})^2(\Delta_\pi - \Delta_{\sigma+})^2}{Z} \quad (14)$$

where

$$Z = 4\Gamma^2(\Delta_\pi - \Delta_{\sigma-})^2(\Delta_\pi - \Delta_{\sigma+})^2 + [4\Delta_\pi(\Delta_\pi - \Delta_{\sigma+})(\Delta_\pi - \Delta_{\sigma-}) - (\Delta_\pi - \Delta_{\sigma+})\Omega_{\sigma-}^2 - (\Delta_\pi - \Delta_{\sigma-})\Omega_{\sigma+}^2]^2$$

And  $\Gamma$  is the total decay rate of the excited state. The bright resonance will appear when

$$4\Delta_\pi(\Delta_\pi - \Delta_{\sigma+})(\Delta_\pi - \Delta_{\sigma-}) - (\Delta_\pi - \Delta_{\sigma+})\Omega_{\sigma-}^2 - (\Delta_\pi - \Delta_{\sigma-})\Omega_{\sigma+}^2 = 0 \quad (15)$$

In the experiment, we control  $\Delta_\pi$  by changing the detuning of the probe beam that has only the  $\pi$ -polarization. The three roots independently correspond to the big Doppler peak and two narrow Fano peaks.

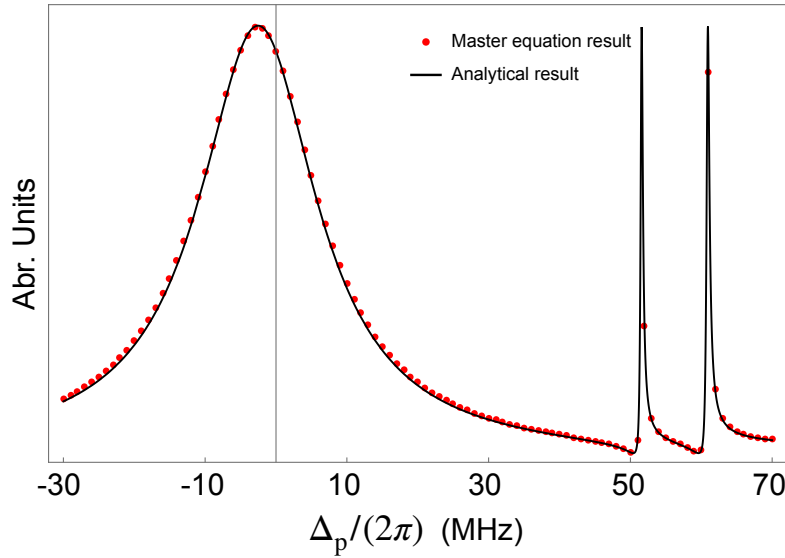


FIG. 5. The spectrum calculated by the master equation and the analytical solution. Here we set  $\Gamma/(2\pi) = 21$  MHz,  $\Delta_{\sigma+}/(2\pi) = 50.4$  MHz,  $\Delta_{\sigma-}/(2\pi) = 59.6$  MHz,  $\Omega_{\sigma-}/(2\pi) = \Omega_{\sigma+}/(2\pi) = 17$  MHz, and  $\Omega_\pi/(2\pi) = 0.5$  MHz. The dot represent the result calculated from the master equation and the curve is calculated by the Eq.(14).

### C. The dressed-states interpretation for the bright resonance

With only the two driving beams and no probe beam, we have the Hamiltonian

$$\hat{H} = \begin{pmatrix} 0 & \frac{\Omega_{\sigma-}}{2} & 0 & \frac{\Omega_{\sigma+}}{2} \\ \frac{\Omega_{\sigma-}}{2} & \Delta_{\sigma-} & 0 & 0 \\ 0 & 0 & 0 & 0 \\ \frac{\Omega_{\sigma+}}{2} & 0 & 0 & \Delta_{\sigma+} \end{pmatrix} \quad (16)$$

The energy of the dressed states can be calculated by diagonalizing the above Hamiltonian, which results in solving the following equation

$$\frac{1}{4}\lambda [4\lambda(\lambda - \Delta_{\sigma+})(\lambda - \Delta_{\sigma-}) - (\lambda - \Delta_{\sigma+})\Omega_{\sigma-}^2 - (\lambda - \Delta_{\sigma-})\Omega_{\sigma+}^2] = 0. \quad (17)$$

These energies of dressed states can be observed by applying a probe beam with  $\pi$ -polarization, as shown in Fig. 6, which is consistent to the result of Eq.(15).

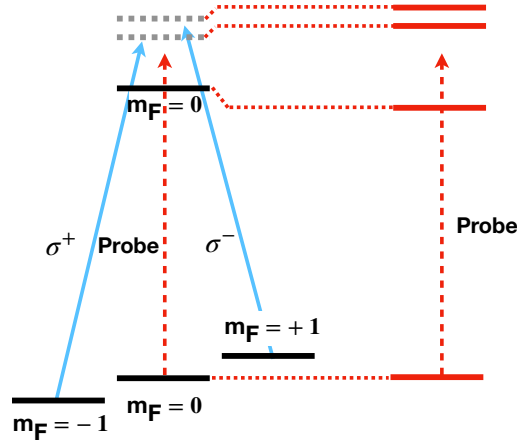


FIG. 6. The dressed states. The gray dotted lines are the energy level without the interaction without the  $\Omega_{\sigma,\pm}$  fields. The red lines are the dressed states formed by the laser field and the atomic levels.

#### D. The master equation treatment for the double-EIT cooling

The Hamiltonian that describes the interaction between the four-level system and the laser fields shown in Fig. 1(a) can be written as

$$\hat{H} = \begin{pmatrix} \omega_{|e\rangle} & \frac{\Omega_{\sigma-}}{2} e^{-i(\vec{k}_d \cdot \vec{r} - \omega_d t)} & -\frac{\Omega_{\pi}}{2} e^{-i(\vec{k}_p \cdot \vec{r} - \omega_p t)} & \frac{\Omega_{\sigma+}}{2} e^{-i(\vec{k}_d \cdot \vec{r} - \omega_d t)} \\ \frac{\Omega_{\sigma-}}{2} e^{i(\vec{k}_d \cdot \vec{r} - \omega_d t)} & \omega_{|+\rangle} & 0 & 0 \\ -\frac{\Omega_{\pi}}{2} e^{i(\vec{k}_p \cdot \vec{r} - \omega_p t)} & 0 & \omega_{|0\rangle} & 0 \\ \frac{\Omega_{\sigma+}}{2} e^{i(\vec{k}_d \cdot \vec{r} - \omega_d t)} & 0 & 0 & \omega_{|-\rangle} \end{pmatrix} \quad (18)$$

where  $\vec{k}_{p(d)}$  and  $\omega_{p(d)}$  are the k-vector and the frequency of the probe (driving) beam and  $\omega_{|e\rangle}, (\omega_{|-\rangle}, \omega_{|0\rangle}, \omega_{|+\rangle})$  are the energies of the corresponding levels. For a rest ion, in the rotating frame the Hamiltonian can be simplified to

$$\hat{H}_s = \begin{pmatrix} 0 & \frac{\Omega_{\sigma-}}{2} & -\frac{\Omega_{\pi}}{2} & \frac{\Omega_{\sigma+}}{2} \\ \frac{\Omega_{\sigma-}}{2} & \Delta_d + \delta_B & 0 & 0 \\ -\frac{\Omega_{\pi}}{2} & 0 & \Delta_p & 0 \\ \frac{\Omega_{\sigma+}}{2} & 0 & 0 & \Delta_d - \delta_B \end{pmatrix} \quad (19)$$

The absorption spectrum can be obtained by numerical solving the steady state solution of the master equation corresponding to the Hamiltonian Eq.(19)

$$\frac{d\hat{\rho}}{dt} = -i[\hat{H}_s, \hat{\rho}] + \mathcal{L}\rho, \quad (20)$$

where  $\mathcal{L}$  is the Lindblad operator corresponding to the three spontaneous decay channel  $\mathcal{L}\rho = \sum_{i=1}^3 c_i \rho c_i^\dagger - \frac{1}{2}[c_i^\dagger c_i, \rho]$  and  $c_1 = \sqrt{\Gamma/3}|+\rangle\langle e|$ ,  $c_2 = \sqrt{\Gamma/3}|0\rangle\langle e|$ ,  $c_3 = \sqrt{\Gamma/3}|-\rangle\langle e|$ .

For the moving ion, the Hamiltonian in the rotating frame can be written as

$$\hat{H}_m = \begin{pmatrix} 0 & \frac{\Omega_{\sigma-}}{2} e^{-i\vec{k}_d \cdot \vec{r}} & -\frac{\Omega_{\pi}}{2} e^{-i\vec{k}_p \cdot \vec{r}} & \frac{\Omega_{\sigma+}}{2} e^{-i\vec{k}_d \cdot \vec{r}} \\ \frac{\Omega_{\sigma-}}{2} e^{i\vec{k}_d \cdot \vec{r}} & \Delta_d + \delta_B & 0 & 0 \\ -\frac{\Omega_{\pi}}{2} e^{i\vec{k}_p \cdot \vec{r}} & 0 & \Delta_p & 0 \\ \frac{\Omega_{\sigma+}}{2} e^{i\vec{k}_d \cdot \vec{r}} & 0 & 0 & \Delta_d - \delta_B \end{pmatrix} \quad (21)$$

In the simulation for the cooling effect, we set  $\vec{k}_d = -\vec{k}_p = \hat{y}$  to deal only the relevant motional mode by the laser beams. For the quantized ion motion in the harmonic potential, the position operator can be decomposed to the creation and the annihilation operator of the phonon  $\hat{y} = \sqrt{\frac{1}{2M\omega_{\text{COM}}}}(\hat{a} + \hat{a}^\dagger)$ , where  $\omega_{\text{COM}}$  is the frequency of the harmonic potential. The cooling speed can be calculated by solving the time evolution of the master equation corresponding to  $\hat{H}_m$  and the cooling limit can be calculated by the average phonon number of the steady state solution of the master equation.

### E. Measurements of Rabi Frequencies of the probe and driving beams

We measure the Rabi frequencies of the probe and driving laser beams by observing Ramsey oscillations from the differential AC-stark shift of the beams. We use the clock qubit and Zeeman qubits to measure all the three components of polarizations, as shown in the Fig.7.

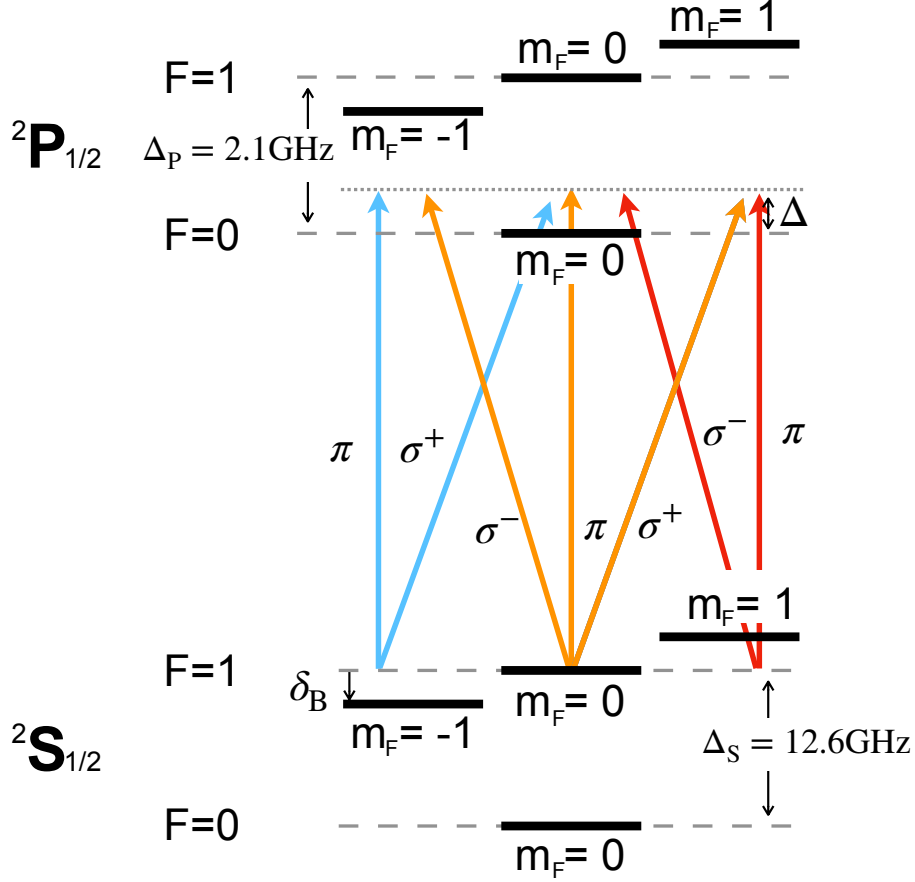


FIG. 7. Energy levels of the  $^{171}\text{Yb}^+$ . The AC stark shift originated from different transitions are labelled by different colors. The blue and red lines corresponding to the transitions contribute to the differential AC stark shift of the Zeeman qubits and the orange lines corresponding to the transitions for the clock qubit.

For the clock state qubit  $^2S_{1/2}|F=0, m_F=0\rangle$  to  $^2S_{1/2}|F=1, m_F=0\rangle$ , the AC-stark is given by the following formula

$$\Delta_{\text{AC}}^{\text{clock}}(\Omega_+, \Omega_-, \Omega_\pi, \Delta) = \Omega_\pi^2 \left( \frac{1}{\Delta} + \frac{1}{\Delta_P + \Delta_S - \Delta} \right) + (\Omega_-^2 + \Omega_+^2) \left( \frac{1}{\Delta_P + \Delta_S - \Delta} - \frac{1}{\Delta_P - \Delta} \right), \quad (22)$$

where the first term comes from the transition  $^2S_{1/2}|F=1, m_F=0\rangle$  to  $^2P_{1/2}|F=0, m_F=0\rangle$  and  $^2S_{1/2}|F=0, m_F=0\rangle$  to  $^2P_{1/2}|F=1, m_F=0\rangle$  while the second term comes from the transition  $^2S_{1/2}|F=1, m_F=0\rangle$  to  $^2P_{1/2}|F=1, m_F=\pm 1\rangle$  and  $^2S_{1/2}|F=0, m_F=0\rangle$  to  $^2P_{1/2}|F=1, m_F=\pm 1\rangle$ . Including the dephasing due to the spontaneous emission whose strength is proportional to the  $1/\Delta^2$ , the Ramsey oscillation can be described by

$$\sin^2[\Delta_{\text{AC}}^{\text{clock}}(\Omega_+, \Omega_-, \Omega_\pi, \Delta)t] \times e^{-\Gamma * \Omega_\pi^2 t / \Delta^2} e^{-\Gamma * (\Omega_-^2 + \Omega_+^2) t / (\Delta_P - \Delta)^2}. \quad (23)$$

In a similar way, Ramsey oscillations of the two Zeeman qubits can be described by

$$\sin^2[\Delta_{\text{AC}}^{\pm 1}(\Omega_+, \Omega_-, \Omega_\pi, \Delta)t] \times e^{-\Gamma * \Omega_\pi^2 t / (\Delta \pm \delta_B)^2} e^{-\Gamma * \Omega_\pi^2 t / (\Delta_P - \Delta)^2}, \quad (24)$$

where  $\Delta_{\text{AC}}^{\pm 1}$  are the differential AC-stark shifts of the Zeeman qubits which are given by

$$\Delta_{AC}^{\pm 1}(\Omega_+, \Omega_-, \Omega_\pi, \Delta) = \Omega_\mp^2 \left( \frac{1}{\Delta \pm \delta_B} - \frac{1}{\Delta_P - \Delta \mp \delta_B} + \frac{1}{\Delta_P + \Delta_S - \Delta} \right) + \Omega_\pi^2 \left( -\frac{1}{\Delta_P - \Delta} + \frac{1}{\Delta_P + \Delta_S - \Delta} \right) + \frac{\Omega_\pm^2}{\Delta_P + \Delta_S - \Delta}. \quad (25)$$

To measure the Ramsey oscillation, we first prepare the ion to its ground state  $^2S_{1/2}|F=1, m_F=0\rangle$  by the optical pumping. Then a Ramsey sequence [43] is applied. To measure the Rabi frequencies of the three components, we run the Ramsey sequence on all of three qubits, where the measurement and fitting results are shown in Fig. 8.

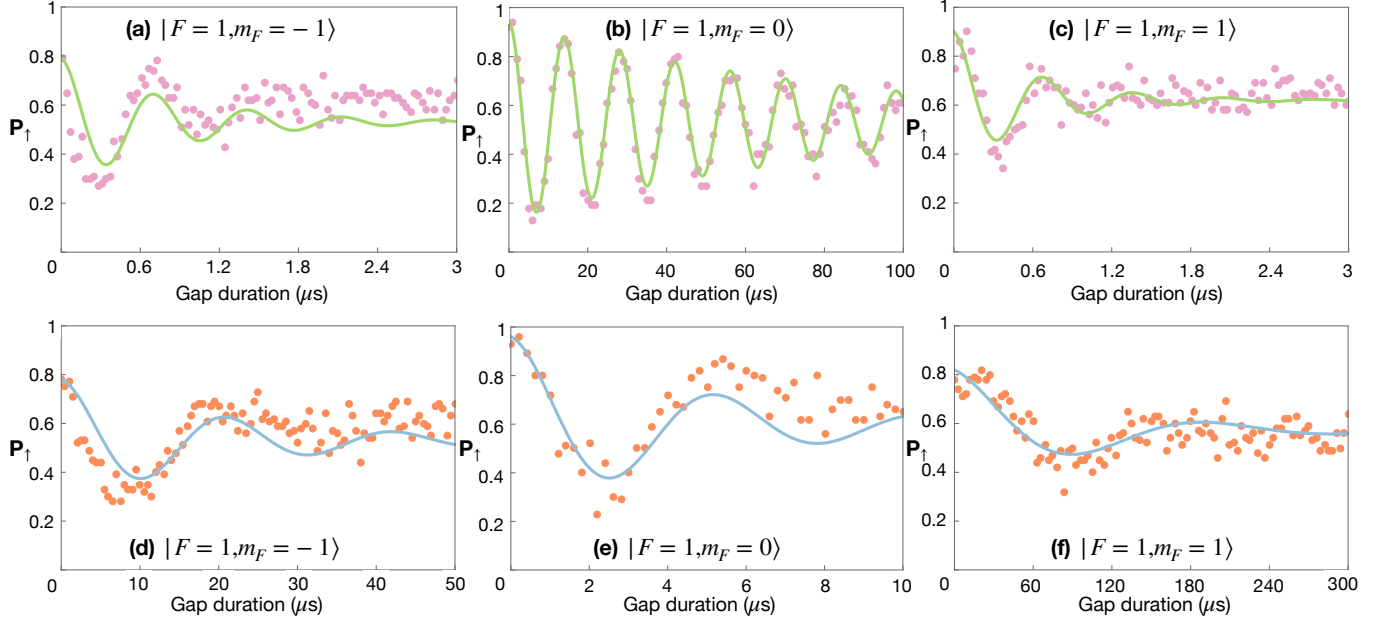


FIG. 8. Results of the Ramsey measurements (a-c) for the driving beam and (d-f) for the probe beam.

We note that the signal of Fig. 8 (b) is used to align the direction of B-field. Once the B-field is parallel to the driving beam, the  $\pi$  component of the driving beam will be eliminated, and the dephasing induced by the spontaneous emission will be reduced.

### F. Extraction of the phonon number from the sideband transitions

In our experiment the states  $|F = 0, m_F = 0\rangle$  and  $|F = 1, m_F = 0\rangle$  in the  $^2S_{1/2}$  manifold, where the energy difference is  $\omega_0$ , are defined as the  $|\downarrow\rangle$  and  $|\uparrow\rangle$  states of the qubit, respectively. A pair of 355 nm laser beams shown in Fig. 1(c) with a frequency difference  $\omega_R$  are used to drive the qubit through the Raman transition [49]. As in the main text, we define  $\mu_R \equiv \omega_R - \omega_0$  as the detuning of the Raman transition relative to the qubit transition.

When the detuning of the transition  $\mu_R$  matches the frequency of a motional mode, the Hamiltonians  $\hat{H}_{r,m}$  and  $\hat{H}_{b,m}$ , which represent the case of  $\mu_R = -\omega_m$  and  $\mu_R = \omega_m$ , respectively, can be written by

$$\hat{H}_{r,m} = \hat{a}_m \sqrt{\frac{1}{2M\omega_m}} \sum_j b_j^m \hat{\sigma}_j^+ + \text{h.c.} \quad (26)$$

$$\hat{H}_{b,m} = \hat{a}_m^\dagger \sqrt{\frac{1}{2M\omega_m}} \sum_j b_j^m \hat{\sigma}_j^+ + \text{h.c.}, \quad (27)$$

where  $M$  is the mass of single  $^{171}\text{Yb}^+$  ion,  $\hat{a}_m^\dagger$ ,  $\hat{a}_m$  and  $\omega_k$  are the creation, annihilation operator and angular frequency of the  $k$ -th motional mode,  $b_j^k$  is the normal mode transformation matrix of the  $j$ -th ion with  $k$ -th mode. After the time evolution  $\hat{U}_{r(b),m}(t)$  of the Hamiltonian with an initial state  $|\downarrow\downarrow\downarrow\cdots\downarrow\rangle|n\rangle_m$ , where  $|n\rangle_m$  is a Fock state of  $k$ -th mode, we can get the time dependence of the normalized average upstate population as

$$P_{\uparrow}^{r(b),m}(t, n) = \text{Tr} \left[ \left( \sum_j \frac{\hat{\sigma}_j^z + \hat{I}_s}{2} \otimes \hat{I}_m \right) \rho_{r(b),m}(t, n) \right] \quad (28)$$

where  $\hat{I}_s$  and  $\hat{I}_m$  are the identity operators of spins and the  $k$ -th mode and  $\rho_{r(b),m}(t, n) = \hat{U}(t)_{r(b),m} |\downarrow\downarrow\downarrow\cdots\downarrow\rangle\langle\downarrow\downarrow\downarrow\cdots\downarrow| \otimes |n\rangle_m\langle n| \hat{U}(t)_{r(b),m}^\dagger$  is the density matrix after the time evolution of duration  $t$ . If we start from a thermal state which is described by the density matrix

$$\rho_{\text{th}}(\bar{n}) = \sum_i \frac{\bar{n}^i}{(\bar{n} + 1)^{i+1}} |i\rangle_m \langle i|_m. \quad (29)$$

Instead of simulating the master equation with this density matrix as initial state, we numerically solve the time evolution from a Fock state with different phonon number and obtain the probabilities of a set  $\{P_{\uparrow}^{r(b),m}(t, 0), P_{\uparrow}^{r(b),m}(t, 1), \dots, P_{\uparrow}^{r(b),m}(t, n)\}$ . Then the average upper-state probability after the time evolution from a thermal state can be calculated by the weighted superposition of each evolution of a Fock state, as shown below equation.

$$P_{\uparrow}^{r(b),m}(t) = \text{Tr} \left[ \left( \sum_j \frac{\hat{\sigma}_j^z + \hat{I}_s}{2} \otimes \hat{I}_m \right) \rho_{r(b),\text{th}}(t, \bar{n}) \right] = \sum_i \frac{\bar{n}^i}{(\bar{n} + 1)^{i+1}} P_{\uparrow}^{r(b),m}(t, i) \quad (30)$$

At the  $\pi$  duration of COM mode, we compare the ratio between blue-sideband and red-sideband transition for the  $k$ -th mode,  $P_{\uparrow}^{r,m}(t)/P_{\uparrow}^{b,m}(t)$  to the Eq. (30). Then we deduce the  $\bar{n}$  for the  $k$ -th mode.

With this method we fit the peaks in Fig. 4(b) and estimate the final temperature after the double-EIT cooling. The fitted results are  $\{0.101$  (zig-zag mode),  $0.0460$ ,  $0.0283$ ,  $0.0817$ ,  $0.0996$ ,  $0.0181$ ,  $0.0759$ ,  $0.0337$ ,  $0.0388$ ,  $0.0495$ ,  $0.0274$ ,  $1.04$  (COM mode) $\}$ .

### G. Thermometry based on the optical-dipole-force

Fig. 9 shows the laser setup for generating the optical-dipole-force(ODF).

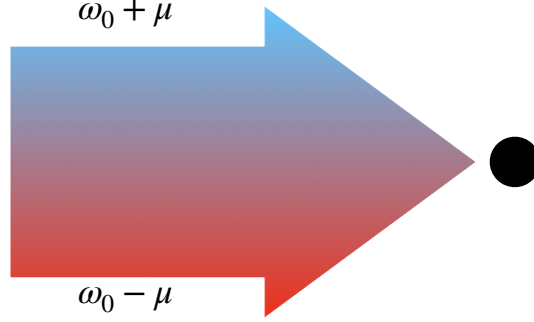


FIG. 9. Laser setting for the ODF measurement.

For the pair of Raman beam, the effective Hamiltonian can be written as

$$H_I^{(\text{eff})} = \sum_j \frac{\Omega_j}{2} e^{-i[\Delta k \cdot r_j(t) - \delta t - \Delta \varphi]} \hat{\sigma}_j^+ + \text{H.c.}, \quad (31)$$

where  $\delta = \omega_R - \omega_0$ ,  $\Omega_j$  and  $\Delta k$  are the Rabi frequency and net wave-vector of Raman laser beams, respectively. If we use two pair of Raman beam to generate two effective coupling simultaneously with opposite detuning  $\mu_R$  for the ODF, the whole Hamiltonian can be written as

$$H_{I,\text{ODF}}^{(\text{eff})} = \sum_j \frac{\Omega_j}{2} e^{-i[\Delta k_1 \cdot r_j(t) - \mu_R t - \varphi_1]} \hat{\sigma}_j^+ + \frac{\Omega_j}{2} e^{-i[\Delta k_2 \cdot r_j(t) + \mu_R t - \varphi_2]} \hat{\sigma}_j^+ + \text{H.c.} \quad (32)$$

Though we have four transitions and two Raman transitions, we typically use only two laser beams. One has only one component, and the other has two frequency components. In this situation we have  $\Delta k_1 = \Delta k_2$ . And we can rewrite the two phase terms by  $\varphi_s = \frac{\varphi_1 + \varphi_2}{2}$  and  $\varphi_m = \frac{\varphi_1 - \varphi_2}{2}$ . Then the Hamiltonian becomes

$$H_{I,\text{ODF}}^{(\text{eff})} = \frac{\Omega_j}{2} (\cos(\Delta k \cdot r_j) + i \sin(\Delta k \cdot r_j)) \cos(\mu_R t + \varphi_m) (\hat{\sigma}_x^{(j)} \cos \varphi_s - \hat{\sigma}_y^{(j)} \sin \varphi_s). \quad (33)$$

In experiment, we calibrate the phase of two different frequency components to be the same,  $\varphi_s = \varphi_m = 0$ , and the  $\Delta k$  along the y direction. Then we have

$$H_I^{(\text{eff})} = \frac{\Omega_j}{2} [\cos(\Delta k \cdot y_j) \cos \mu_R t + i \sin(\Delta k \cdot y_j) \cos \mu_R t] \hat{\sigma}_x^{(j)}, \quad (34)$$

where the first term gives us the dephasing dependent on the motional state along the x-axis in the Bloch sphere [45]:

$$P_{\uparrow}^j = \frac{1}{2} \left[ 1 - e^{-2\Gamma_D \tau} \exp \left( -2 \sum_m |\alpha_{jm}|^2 (2\bar{n}_m + 1) \right) \right], \quad (35)$$

where  $\Gamma_D$  describes the decoherence in the experiment and

$$\alpha_{jm} = \frac{\Omega_j b_{jm}}{(\mu_R^2 - \omega_m^2)} \sqrt{\frac{1}{2M\omega_m}} (\omega_m(1 - \cos \phi) + i\mu_R \sin \phi - e^{i\omega_m \tau} \{ \omega_m [\cos(\mu_R \tau) - \cos(\mu_R \tau + \phi)] - i\mu_R [\sin(\mu_R \tau) - \sin(\mu_R \tau + \phi)] \}), \quad (36)$$

where  $\phi = (\tau + \tau_\pi)(\mu_R - \omega_m)$  and  $\tau_\pi$  is the duration for the  $\pi$ -pulse during the ODF measurement. For the relative long duration of the ODF pulse we have  $\phi \approx \tau(\mu_R - \omega_m)$

The spectrum resulting from the Eq.(36) with different phonon number are shown in 10(a). The null point corresponding to  $\tau(\mu_R - \omega_m) = 2n\pi$ . In the experiment we individually detect the fluorescence of ions in the crystal to get the downstate population and measure the strength of ODF by the Rabi oscillation of the carrier transition.

We develop a convenient way to study the cooling dynamics without obtaining the spectroscopy signal of Fig. 10(a) at each step of the cooling. We fix the detuning of the ODF beams at the highest peak of the spectrum shown in the dashed line of Fig. 10(a), which is  $(\mu_R - \omega_{\text{COM}})\tau_{\text{ODF}}/(2\pi) = 0.37$  in our experiment, and record the up-state probability during the cooling. As shown in Fig.10(a), with the same strength and duration of the ODF beams, the decrease of the temperature will lower the height of the spectrum.

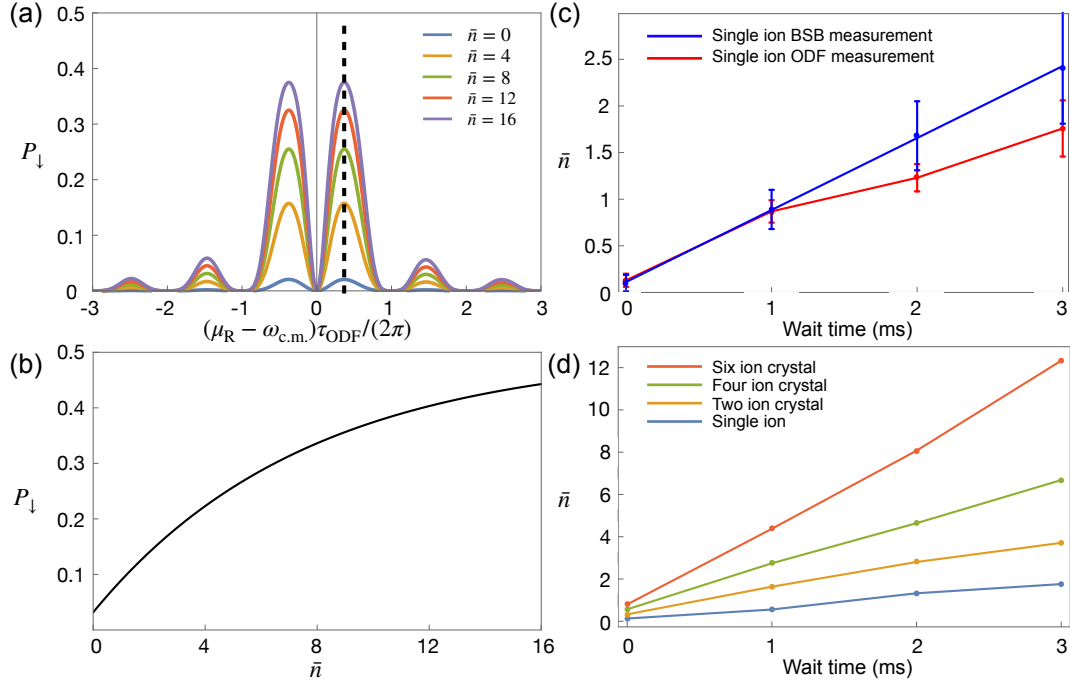


FIG. 10. ODF spectrum and the heating measurement. (a) The ODF spectrum of average up-state population with different phonon number for the COM mode. The dashed black line indicates the chosen detuning to measure the average phonon number. (b) The relation between the average phonon number and the average downstate population at the detuning of ODF pulse indicated in (a). (c) Comparison of the results of heating measurements between blue-sideband (blue line) and ODF height method (red line). (d) The heating measurement of multiple ions by the ODF height method.

The relation between the up-state probability at the chosen detuning and the temperature is shown in the Fig.10(b). By fitting the experimentally measured  $P_{\uparrow}$  to the corresponding function, we can quickly obtain the temperature of the mode, which we name as ODF height method. The reliability of this method is verified with the blue-sideband measurement for the heating of a single ion. We first measure the heating rate of a single ion by both the blue-sideband method and the ODF height method. Then we compare their results, which are consistent, as shown in Fig.10(c). Then we apply the ODF height method to measure the heating rate for COM mode of 2D crystals consisted of 2, 4, 6 and 12 ions. As shown in Fig.10(d), the heating rate for the COM mode increases linearly with the number of ions as expected.

Fig.11 shows the cooling dynamics for the 2D crystal with different number of ions by using the ODF height method.



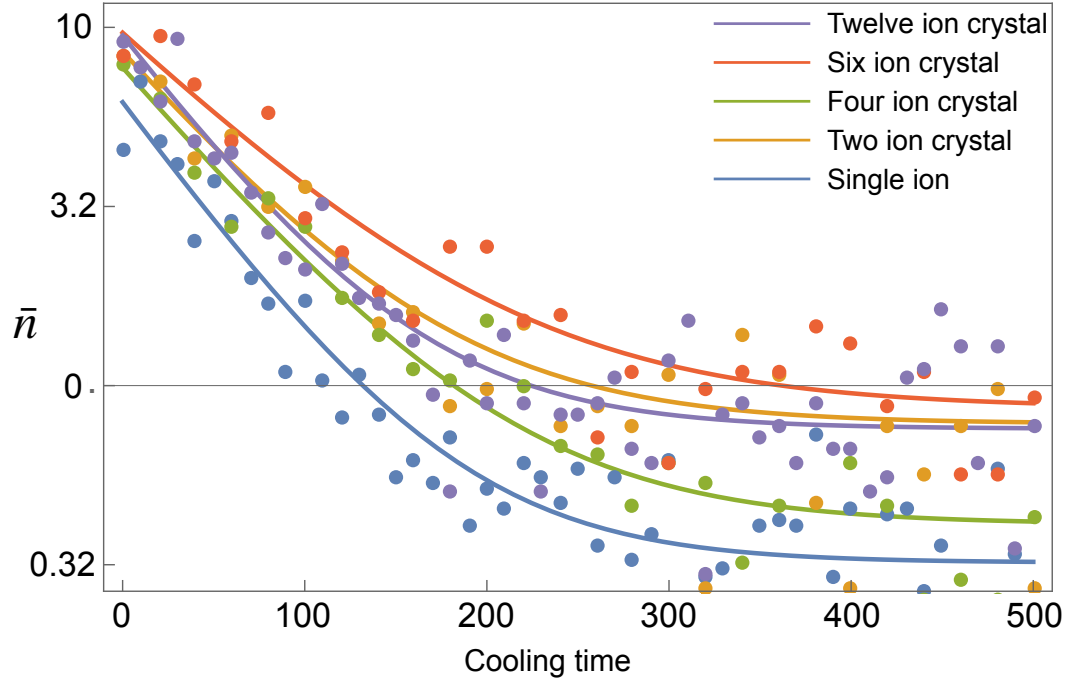


FIG. 11. Multi-ion crystal heating measurement by the ODF height method for 2, 4, 6 and 12 ions.